Bioactive Materials 43 (2025) 225–239

Contents lists available at ScienceDirect

Bioactive Materials

journal homepage: www.keaipublishing.com/en/journals/bioactive-materials

Semi-quantitative elemental imaging of corrosion products from bioabsorbable Mg vascular implants *in vivo*

Weilue He [a], Keith W. MacRenaris [b,c,d], Adam Griebel [e], Maria P. Kwesiga [f], Erico Freitas [g], Amani Gillette [h], Jeremy Schaffer [e], Thomas V. O'Halloran [b,c,d], Roger J. Guillory II [i,*]

[a] Department of Biomedical Engineering, Michigan Technological University, USA
[b] Department of Microbiology, Genetics and Immunology (MGI) and Chemistry, Michigan State University, USA
[c] Elemental Health Institute (EHI), Michigan State University, USA
[d] Quantitative Bio-Element Analysis and Mapping (QBEAM) Center, Michigan State University, USA
[e] Fort Wayne Metals, Fort Wayne, IN, USA
[f] Department of Biomedical Sciences, Grand Valley State University, USA
[g] Department of Materials Science and Engineering, Michigan Technological University, USA
[h] Department of Biomedical Engineering, Morgridge Institute for Research, USA
[i] Joint Department of Biomedical Engineering, Medical College of Wisconsin, Marquette University, USA

A B S T R A C T

While metal materials historically have served as permanent implants and were designed to avoid degradation, next generation bioabsorbable metals for medical devices such as vascular stents are under development, which would elute metal ions and corrosion byproducts into tissues. The fate of these eluted products and their local distribution in vascular tissue largely under studied. In this study, we employ a high spatial resolution spectrometric imaging modality, laser ablation inductively coupled plasma time-of-flight mass spectrometry (LA-ICP-TOF-MS) to map the metal distribution, (herein refered to as laser ablation mapping, or LAM) from Mg alloys within the mouse vascular system and approximate their local concentrations. We used a novel rare earth element bearing Mg alloy (WE22) wire implanted within the abdominal aorta of transgenic hypercholesterolemic mice (APOE−/−) to simulate a bioabsorbable vascular prosthesis for up to 30 days. We describe qualitatively and semi-quantitatively implant-derived corrosion product presence throughout the tissue cross sections, and their approximate concentrations within the various vessel structures. Additionally, we report the spatial changes of corrosion products, which we postulate are mediated by phagocytic inflammatory cells such as macrophages (MΦ's).

1. Introduction

It has been recognized that a temporary implant is potentially more clinically beneficial vs. its permanent implant counterpart for certain applications such as vascular and orthopedic medical devices [1]. First generation bioabsorbable materials were polymer based, such as polyethylene glycol (PEG), poly-L-lactic acid (PLLA), and poly (lactic-co-glycolic acid) (PLGA), and were introduced for use in the clinic more than 50 years ago [2]. Due to their inferior mechanical properties, the application of polymer-based materials for complex loading situations is limited, whereas bioabsorbable metals have become a promising alternative for implantable devices over the last few decades [3]. One of the most challenging clinical applications of bioabsorbable metal materials is for vascular stenting [4]. The resorption of the metal over time allows for regeneration and repair of damaged vascular tissue that can fully restore function to the vessel, alleviate long term complications such as very late stent thrombosis, and neoatherosclerosis [5]. To date, the most explored bioabsorbable metal material for vascular stenting is magnesium (Mg). The first generation of bioabsorbable metal stents were made for clinical use from a Mg alloy with a balance of rare earth elements (REEs), based on the WE43 alloy formulation (93 % Mg, 3–4% Yttrium (Y), 3–4% other REEs) (Magmaris®, Biotronik) [6]. Grain refinement, solid solution strengthening, and particle dispersion strengthening via the addition of REEs to Mg have been the dominant pathways of increasing ductility and strength of typically brittle and weak pure Mg [7].

Peer review under responsibility of KeAi Communications Co., Ltd.

* Corresponding author. Joint Biomedical Engineering Department, Medical College of Wisconsin & Marquette University, Milwaukee, WI, 53223, USA.
E-mail addresses: weilueh@mtu.edu (W. He), macrenar@msu.edu (K.W. MacRenaris), adam_griebel@fwmetals.com (A. Griebel), kwesigam@gvsu.edu (M.P. Kwesiga), efragafr@mtu.edu (E. Freitas), agillette@wisc.edu (A. Gillette), jeremy_schaffer@fwmetals.com (J. Schaffer), ohallor8@msu.edu (T.V. O'Halloran), rguillory@mcw.edu (R.J. Guillory II).

https://doi.org/10.1016/j.bioactmat.2024.07.023
Received 31 January 2024; Received in revised form 18 June 2024; Accepted 15 July 2024

As Mg alloys gained use as bioabsorbable metals, concerns regarding the biocompatibility of non-endogenous elements grew [8–10]. In a landmark study by Feyerband *et al.* in 2010, the first recommendations were made in the general use of REEs based on *in vitro* cytotoxicity assays. It was found that cationic lanthanum (La), cerium (Ce), neodymium (Nd), and praseodymium (Pr) were particularly toxic with increasing concentrations, whereas yttrium (Y), gadolinium (Gd), and dysprosium (Dy) were less toxic [11]. Additionally, it has also been shown that REEs can upregulate expression of inflammatory genes in smooth muscle cells [12]. While these *in vitro* studies offered insight into general toxicity, little work has been done on evaluating *in vivo* distribution patterns of REEs. Critically, *in vivo* concentrations of REEs near the interface of the material and throughout the tissue has been difficult to determine, allowing for little to no connection on *in vitro* toxicity with *in vivo* biocompatibility. Recent efforts have attempted to describe the *in situ* local accumulation and diffusion of REEs with spectroscopic and spectrometric approaches. Since Mg alloys have advanced significantly in their development for orthopedic applications, most of our knowledge about the diffusion of exogenous metals in tissue originates from implants in bone and joint tissues [13–18]. One exceptional example is a study performed by Amerstofer *et al.*, where laser ablation mass spectrometry (LA-ICP-MS) was employed to evaluate Y diffusion from transcortical WZ21 screws implanted in rat femurs [14]. It was found that Y was detected as far as 1500 μm from the implant interface at 9 months. The relative distance of REE migration from Mg implants in soft tissue such as arteries, remains undetermined.

To date, little is known about the spatial distribution of REE based corrosion products *in situ* within vessels, or their relative concentrations. In this study, a high spatial resolution spectrometric imaging modality termed laser ablation inductively coupled plasma time-of-flight mass spectrometry (LA-ICP-TOF-MS, herein referred to as laser ablation mapping, or LAM), is used to analyze the REE distribution from Mg alloys within the mouse vascular system and approximate their local concentrations. A REE bearing WE series Mg alloy (WE22) wire was implanted within the abdominal aorta of transgenic hypercholesterolemic mice (APOE−/−) to simulate a bioabsorbable vascular prosthesis under pathological conditions for up to 30 d. The APOE−/− mouse was chosen due to its clinically relevant presentation of lipid filled plaques and increased inflammatory responses towards implanted vascular materials [19,20]. WE22 was selected due to its alloy similarity to commercially available WE43, yet lower REE contents, which may be more biocompatible. Here, the qualitative and semi-quantitative features of implant-derived corrosion product presence throughout the tissue cross sections, and their approximate concentrations within the various vessel structures are explored. Corrosion products derived from Mg biocorrosion have been shown to interact directly with macrophages (MΦ's) and inflammatory signaling *in vitro* [21–25]. Additionally, the spatial variability of REE's, which is postulated to be correlated with phagocytic inflammatory cells such as MΦ's, is described in detail.

2. Methods

2.1. Wire fabrication

WE22 (Mg–2Y-1.5Nd-0.5Zn) wires were produced by vacuum induction melting and casting a 50 mm ingot with inputs of magnesium (99.98 % pure), yttrium (99.5 % pure), neodymium (99.5 %) and zinc (Zn) (99.99 %). The ingot was homogenized and extruded to 12.7 mm diameter, then drawn to fine wire using conventional drawing and annealing practices. The wire was annealed at 0.2 mm diameter and then cold drawn to 0.1 mm diameter, imparting 75 % cold work. The 0.1 mm wire was then straightened through a stress-relief treatment at 350 °C to facilitate insertion. Homogenization was carried out at 500 °C for 16 h. Extrusion was implemented at a temperature of 450 °C, using methodology similar to prior work [26].

2.2. In vivo implantation

All protocols for this animal model were approved by the Animal Care and Use Committee of Michigan Technological University. Wires were implanted into the abdominal aorta of three 6-month-old APOE−/− transgenic mice (Charles River Laboratories) using methods previously described elsewhere [27,28]. We began the experiments with animal numbers at n = 3. One animal was euthanized after 24 h due to procedure related complications. The remaining two animals successfully survived until 30 d implantation and were evaluated for this study. The 24 h timepoint was only evaluated for scanning electron microscopy (SEM) imaging (Fig. 1). Multiple sections from 30 d explants (n = 2) were evaluated with LAM and SEM. One 30 d specimen was processed for high resolution transmission electron microscopy (HR-TEM).

2.3. Tissue collection and preparation

The vascular tissue containing the wire was collected after euthanasia by cutting the proximal and distal ends of the aorta-vena cava bundle. The tissue was placed into cryomolds and surrounded by OCT media and snap frozen in liquid nitrogen. Samples were cryo-sectioned (10 μm thick) with a HM525 cryomicrotome at −20 °C, and warm collected onto HistoBond® slides. After the warm collection, samples were immediately stored at −80 °C for further processing.

2.4. Electron microscopy

After tissue sections were collected, the bulk wire-tissue samples were warmed and dehydrated in 200 proof ethanol for 1 h. Samples were then vacuum dried at 1×10^{-5} mbar overnight. The wire segments were embedded in epoxy resin and processed via standard metallographic processing using an ascending grit series grinding and polishing procedure. The epoxy pucks were coated with a 20 nm carbon coating and imaged with a Phillips XL scanning electron microscope (SEM) equipped with an energy-dispersive X-ray spectroscopy (EDX) system. All x-ray maps were taken with an accelerating voltage >15 kV. After SEM-EDX analysis, the pucks were trimmed with a razor blade and ultra-thin sections were made using a Leica Ultracut UCT ultramicrotome at room temperature. The ribbon of sections was floated and placed onto a lacey carbon coated copper TEM grid. The samples were imaged on an FEI Titan Themis S-TEM. High resolution TEM (HRTEM),electron energy loss spectroscopy (EELS) mapping, and high- angle annular dark field imaging (HAADF) were performed.

2.5. LAM

2.5.1. Custom gelatin standard preparation

Two sets of homogeneous 10 % (m/v) gelatin calibration standards were prepared. Porcine gelatin with 300 bloom strength was used for all gelatin preparations. Gelatin standards were made by diluting a 5000 μg/mL Ce, Dy, Eu, La, Nd, Y multi-element standard (in 2 % v/v nitric acid/trace hydrofluoric acid) and a 1000 μg/mL multi-element standard containing Ca, K, Ba, B, Cr, Cu, In, Pb, Mn, Ag, Sr, Zn, Mg, Al, Bi, Cd, Co, Ga, Fe, Li, Ni, Na, and Tl (IV-Stock-IV, in 5 % v/v nitric acid) into 4.5 mL of ultrapure, deionized water (18.2 MΩ cm at 25 °C) at 65 °C and adding ~ 0.5 g of gelatin (see components in Supplement Table 1). Gelatin standards were then mixed gently using metal free plastic spatulas and degassed in an ultrasonic water bath set at 65 °C to remove any air bubbles from mixing. The gelatin standard was then serially diluted into fresh 10 % (w/v) gelatin in ultrapure deionized water to make 50, 25, 15, 7.5, 1.4, and 0 μg/g elements.

2.5.2. ICP Triple Quadrupole mass spectrometry (ICP-QQQ-MS) trace analysis of stock 2 gelatin standards

Gelatin standards were analyzed using an Agilent 8900 Triple Quadrupole ICP-MS (Agilent, Santa Clara, CA, USA) equipped with the

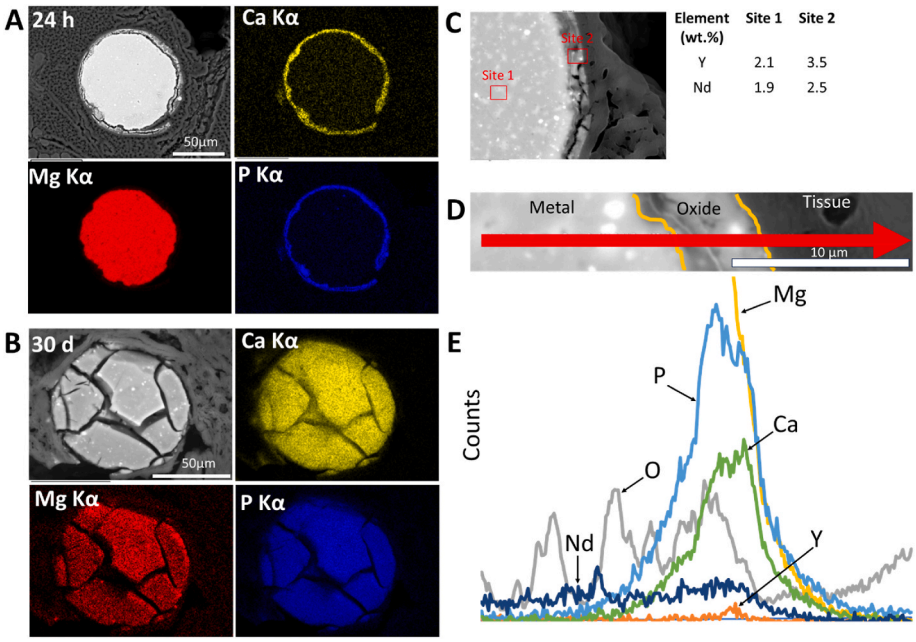

Fig. 1. SEM-EDX characterization of WE22 implants isolated from mouse abdominal aortas 24h (A) and 30 d after implantation (B). Image shown in (C) describes two sites of selected area EDX analysis located in the material bulk (Site 1) and oxide film (Site 2). Graphic in (D) shows placement of a line profile which is detailed by elements in (E).

Agilent SPS 4 Autosampler, integrate sample introduction system (ISiS), x-lens, and micromist nebulizer. Daily tuning of the instrument was accomplished using the manufacturer supplied tuning solution containing Li, Co, Y, Ce, and Tl. Global tune optimization was based on optimizing intensities for ^{7}Li, ^{89}Y, and ^{205}Tl while minimizing oxides (^{140}Ce^{16}O/^{140}Ce < 1.5 %) and doubly charged species (^{140}Ce++/^{140}Ce+ < 2 %). Following global instrument tuning, gas mode tuning in He KED and O_2 mode was accomplished using the same manufacturer supplied tuning solution. In KED mode (using 100 % UHP He, Airgas), intensities for ^{59}Co, ^{89}Y, and ^{205}Tl were maximized while minimizing oxides (^{140}Ce^{16}O/^{140}Ce < 0.5 %) and doubly charged species (^{140}Ce++/^{140}Ce+ < 1.5 %) with short term RSDs <3.5 %. In O_2 mode (using 100 % UHP O_2, Airgas) intensities for ^{59}Co, ^{89}Y, and ^{205}Tl with short term RSDs <3.5 %. ICP-MS standards were prepared from a stock solution of IV-Stock-4 multi-element standard (Ca, K, Ba, B, Cr, Cu, In, Pb, Mn, Ag, Sr, Zn, Mg, Al, Bi, Cd, Co, Ga, Fe, Li, Ni, Na, and Tl) as well as multi-element standard containing Ce, Dy, Eu, La, Nd, Y, and Ti (Inorganic Ventures, Christiansburg, VA, USA) that were diluted with 3 % (v/v) trace nitric acid in ultrapure deionized water to a final element concentration of 1000, 100, 10, 1, 0.1, 0.01, and 0 (blank) ng/g standard. Internal standardization was accomplished inline using the ISIS valve and a 200 ng/g internal standard solution in 3 % (v/v) trace nitric acid in ultrapure water consisting of Nb (Inorganic Ventures, Christiansburg, VA, USA) (Supplement Table 2). The isotopes selected for analysis were ^{23}Na, ^{24}Mg, ^{27}Al, ^{39}K, ^{52}Cr, ^{55}Mn, ^{57}Fe, ^{59}Co, ^{60}Ni, ^{65}Cu, ^{66}Zn, ^{71}Ga, ^{88}Sr, ^{89}Y, ^{109}Ag, ^{111}Cd, ^{115}In, ^{137}Ba, ^{139}La, ^{140}Ce, ^{143}Nd, ^{153}Eu, and ^{163}Dy with ^{93}Nb used for internal standardization.

2.5.3. Gelatin standard sectioning protocol

After making 5 gelatin standards (including one blank gelatin solution), the gelatin was prepared for cryosectioning using a Leica CM 3050 S (Leica Biosystems, Deer Park, IL, USA) cryostat. After the gelatin is dissolved and the solution is still at 55 °C, approximately 300 μL of warmed gelatin standard was pipetted onto a precooled chuck inside the cryostat (−20 °C). Gelatin was allowed to freeze for no less than 4 min at −20 °C. Once the gelatin standards were completely frozen, we sectioned sample with a −21 °C chamber temperature and −20 °C objective temperature (temperatures were adjusted slightly depending on the quality of the sections and whether the section stuck to the blade or anti-roll plate) and a section thickness of 10 μm to match the section thickness of the tissue. Gelatin sections were then transferred to precleaned charged microscope slides (Superfrost plus, Thermo scientific) and kept at −20 °C until laser ablation.

2.5.4. LAM instrument setup and sample parameters

Glass slides were loaded into a Bioimage 266 nm laser ablation system (Elemental Scientific Lasers, Bozeman, MT, USA) which is equipped with an ultra-fast low dispersion TwoVol3 ablation chamber and a dual concentric injector (DCI3) and is coupled to an icpTOF S2 (TOFWERK AG, Thun, Switzerland) ICP-TOF-MS. Daily tuning of the LAM settings was performed using NIST SRM612 glass certified reference material (National Institute for Standards and Technology, Gaithersburg, MD, USA). Optimization for torch alignment, lens voltages, and nebulizer gas flow was based on high intensities for ^{140}Ce and ^{55}Mn while maintaining low oxide formation based on the ^{232}Th^{16}O+/^{232}Th + ratio (<0.5). A list of instrument parameters for LAM is summarized in Supplement Table 3. In short, 10 μm thick gelatin standards (5 standards and a blank) were placed directly on charged slides. These 2 slides were loaded with a sample slide which were warmed to RT and immediately exposed to −20 °C cold 200 proof ethanol for 30 s. Sections were dried in a fume hood overnight and then loaded onto the LA sample holder and loaded into the LA system. The system is purged for 5 min with He gas, and patterns are selected on the standards and samples of interest using ActiveView 2 software (ESL, Bozeman, MT, USA). For gelatin standards, 9 lines going across each standard and the blank were drawn using the same laser parameters as the samples (Supplement Table 3). Specifically, 5 μm circular laser spot sizes at 80 % laser power and 100 Hz repetition rate were used with an interline distance 4 times greater than the spot size. This allowed for clean ablation of individual lines without overlap. For the sample, reference points were made around the sample and the aforementioned laser parameters were used with an interline distance equal to the laser spot with no overlap to sample the entire tissue.

2.5.5. Data acquisition and analysis of LAM data

Data was recorded using TofPilot 1.3.4.0 (TOFWERK AG, Thun,

Switzerland). The LAM data were saved in the open-source hierarchical data format (HDF5). Post-acquisition data processing was performed with Tofware v3.2.0, which is a TOFWERK data analysis package and used as an add-on on IgorPro (Wavemetric Inc., OR, USA). The data processing comprised the following steps: (1) drift correction of the mass peak position in the spectra over time via time-dependent mass calibration, (2) determining the peak shape, and (3) fitting and subtracting the mass spectral baseline. The data was further processed with iolite version 4.8.6 (Elemental Scientific Lasers, Bozeman, MT, USA). For calibration, signal responses for each ablation line per gelatin standard were fit to a linear regression and spline auto smoothed. Calibration curves are then generated and using 3D trace elements inside of DRS in Iolite, we can convert integrated counts per second to μg/g (using the previous calculations for the gelatin standards via ICP).

2.6. Data analysis

LAM raw data was stored using a.h5 file and visualized by iolite 4 software in.io4 data format. After manually defining the baseline according to time series data using the "Total Beam" channel, baseline subtraction was performed under the data reduction scheme outlined in iolite. The generated CPS signals for each channel were used for elemental map visualization. As phosphorus (P) is one of the major elements in cellular and tissue constituents, ^{31}P mapping was used to provide tissue and corrosion product contrast. To further determine the uncorroded wire location, ^{56}Fe maps were used due to the low Fe content of the WE22 alloy (Table 1). Specifically, to select the corrosion degradation regions where ^{56}Fe signal is not visible when upper pixel value limits were set to be the 90 % percentile. The vicinity tissues were selected manually based on their relative locations, and P as well as Fe mapping. LAM raw data including all channels of interest corresponding to the designated areas were exported. An imaging area that excludes tissue was selected as the control area, from which the base-line level of each channel was determined by using:

$$BS = 3 \times s$$

where *BS* is the baseline of designated channel and *s* indicates sample standard deviation of the corresponding channel. Base-line values were added to the raw data to generate base-line adjusted data, which ensures all pixel values are positive numbers. The ^{89}Y/^{143}Nd ratio calculation and plotting were performed using base-line adjusted data. R (Version 4.3.2) programming language was used for 2D plotting, 3D plotting, principal component analysis (PCA), and hierarchical clustering. Specifically, before PCA and clustering, data was normalized through data standardization, converting each original value into a z-score. Specifically,

$$Normalized\ data = \frac{x - mean}{s}$$

where x is the raw data; *mean* is the sample mean; and s is the sample standard deviation. The correlation matrix was built according to the normalized data and visualized after hierarchical cluster analysis. The hierarchical cluster analysis was performed based on the scaled raw data. PCA was performed by using FactoMineR package and visualized through factoextra package. It is also required to use other packages to accomplish PCA and data visualization, including: ggplot2, corrr, ggcorrplot, FactoMineR, factoextra, devtools, and ggfortify.

2.7. Statistical analysis

Spearman correlation was calculated with R programming and the results were indicated by the coefficient ρ and the p value, where it was determined to be statistically significant when $p < 0.01$. For comparisons of the quantitative data,Brown-Forsythe and Welch ANOVA tests were performed with a post hoc Dunnett's multiple comparison test executed between groups.

3. Results

3.1. Explant corrosion product characterization

The explant corrosion progression is outlined in Fig. 1, which shows SEM-EDX characterization of wire implants 24 h (Fig. 1A–C, D, and E) and 30 d (Fig. 1B) post-implantation. There was a rapid corrosion layer approximately 5–10 μm thick generated after 24 h. The layer consisted primarily of Ca, P, and was homogenous in thickness around the circular cross section. The line scan presented in Fig. 1D and E shows the transition from the metallic matrix to corrosion layer, with Y and Nd presence within the corrosion film that is seen on REE Mg alloys [7,29–31]. At 30 d post implantation, the entire wire has fully converted into a Ca–P–Mg–O corrosion product, which is shown in Fig. 1B, completely encompassing the original wire metal cross section.

In order to further characterize the corrosion product, HR-TEM and STEM-EELS/EDX of the corrosion products from the 30 d *in vivo* implants were performed. Fig. 2A represents HR-TEM of a selected field within the corrosion product, showing distinct intermetallic particles/phases outlined in red (IMP) in addition to a nanopowder substance surrounding the IMP's. The selected area electron diffraction (SAED) pattern of the region given in Fig. 2A shows three broad diffraction rings. The line profile shows they are centered around 3.0, 4.9, and 8.8 nm^{-1}, which correspond to the d-spacings of 0.33 nm. 0.20 nm, and 0.11 nm, respectively. This matches with amorphous-like (Nd, Y)$_2$O$_3$. Electron diffraction simulation (not shown) suggests the size of the nanoparticle substance surrounding the IMP's is about 1–2 nm. Small diffraction spots in the SAED pattern were observed, originating from the small crystalline IMP's [32]. Interrogation of the IMP's via EDX reveals that they are a mixture of Nd and Y rich particles (Fig. 2B). Oxygen content is seen throughout due to spontaneous oxidation of the sample either in air or the water bath during sample preparation. An image field only containing the nano substance (Fig. 2C) was evaluated with high resolution EELS mapping in Fig. 2D. A combination of yttrium oxide and neodymium oxide was detected via the Y M edge and Nd_2O_3 N edge in comparison to reference spectra (Fig. 2I). The EDX panels in Fig. 2E and F outline distinct IMP's, each with different total counts of Y and Nd. A macroscopic view that includes the EDX scanned region in Fig. 2B is given in Fig. 2G, and spectra are given in Fig. 2H. The images detail the variable sizes of electron dense fine IMP's ranging from 100 nm to above 500 nm. In this disease implant model, the WE22 alloy produced a mixed rare earth nano-oxide (1–2 nm) with variably sized dispersed IMP's (100–500 nm) (Figs. 1 and 2). It was found that the nano substance was likely a mixture of Y_2O_3 and Nd_2O_3 via EELS (Fig. 2D and I) and the IMP's possessed variable counts of Nd and Y (Fig. 2E and F), alluding to different phases. The high Cu content seen in the EDS spectra given in Fig. 2H is due to the copper grid that was used to place sections.

Table 1
Elemental composition of WE22 alloy stock characterized by inductively coupled plasma-atomic emission spectroscopy (ICP-AES).

Element	Mg	Y	Nd	Zn	Mn	Fe	Cu	Ti	Ca
Wt.%	Bal	2.04	1.35	0.5	0.02	<10 ppm	<10 ppm	<10 ppm	<0.01

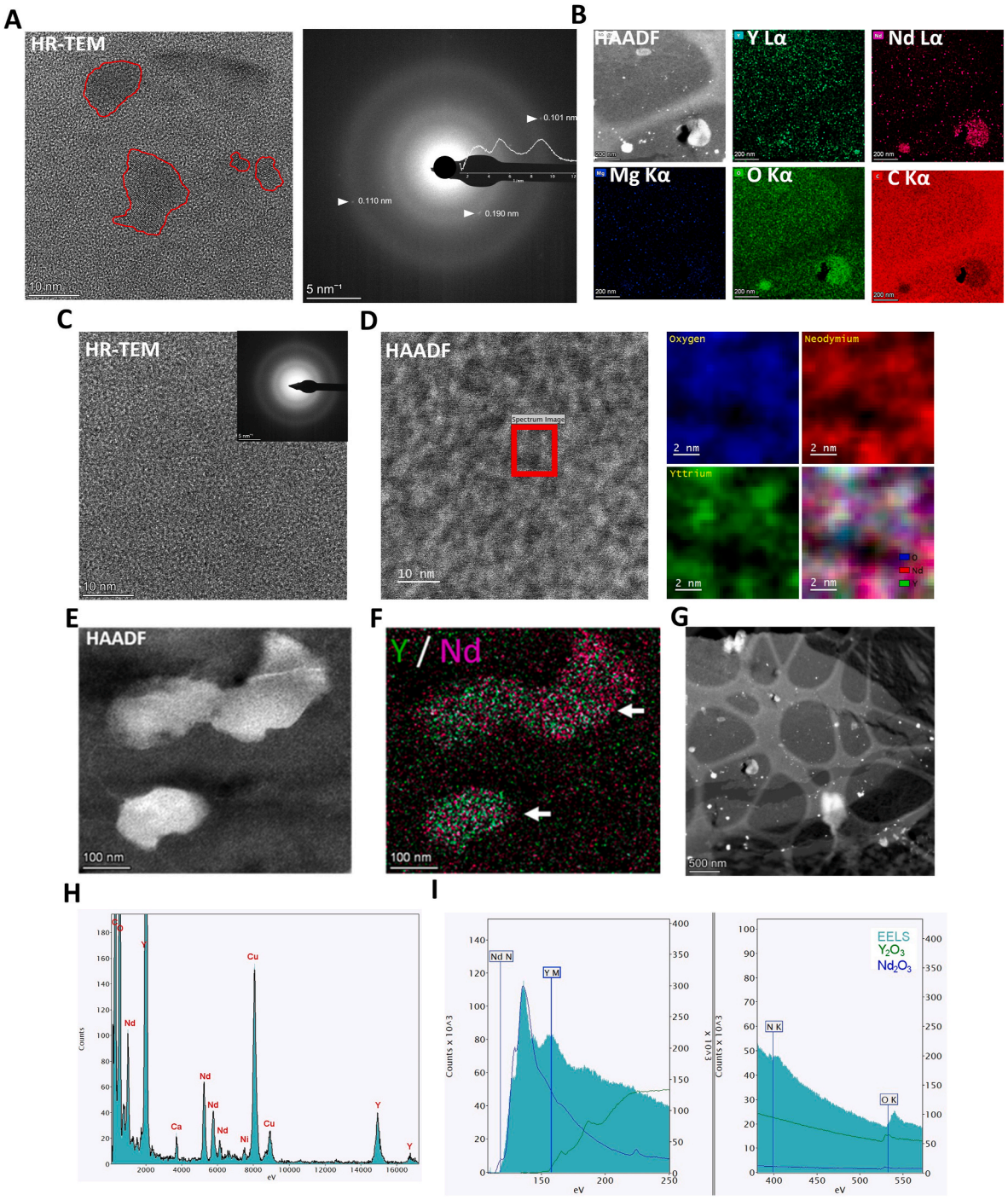

Fig. 2. HRTEM and STEM-EELS/EDX characterization of the corrosion product from WE22 implants on Day 30 post-implantation. Two distinct corrosion products are observed, variably sized crystalline IMP's (A–B) surrounded by a nanopowder substance (C–D). (E–F) High resolution STEM-EDX of IMP's. (G) A macroscopic view of the high-angle annular dark-field (HAADF) region presented in (B). (H–I) EDX and EELS spectra taken from the region presented in (E).

3.2. Qualitative LAM

3.2.1. Survey tissue scans

Scans from LAM of the entire arterial cross sections of the 30 d implants reveal the spatial distribution of endogenous elements and implant derived elements (Fig. 3). Major tissue elements such as ^{31}P, ^{23}Na, and ^{56}Fe outline much of the tissue cross section, providing sufficient elemental contrast to identify histological structures (such as vascular wall, neointima, surrounding tissues, and lymph nodes). The original position of the wire is clearly seen by identification of the ^{26}Mg, ^{89}Y, and ^{146}Nd signals. Different pixel intensity cut-off values can be set to visualize the section (Supplement Fig. 1). Examples of minor impurities and trace elemental REE's of the wire shown in Fig. 3 are given by ICP-QQQ detection given in Table 2.

3.2.2. Trace and abundant REE cluster behavior

To understand the multidimensional dataset, hierarchical clustering (h-clustering) and PCA were performed, and the correlations between each channel across the regions that represent both the corroded implant and animal tissues were visualized in Fig. 4A. The initial h-cluster analysis of the entire tissue scan reports a strong clustering and high correlation of ^{89}Y and ^{143}Nd, as well as other REE's (Fig. 4A). To

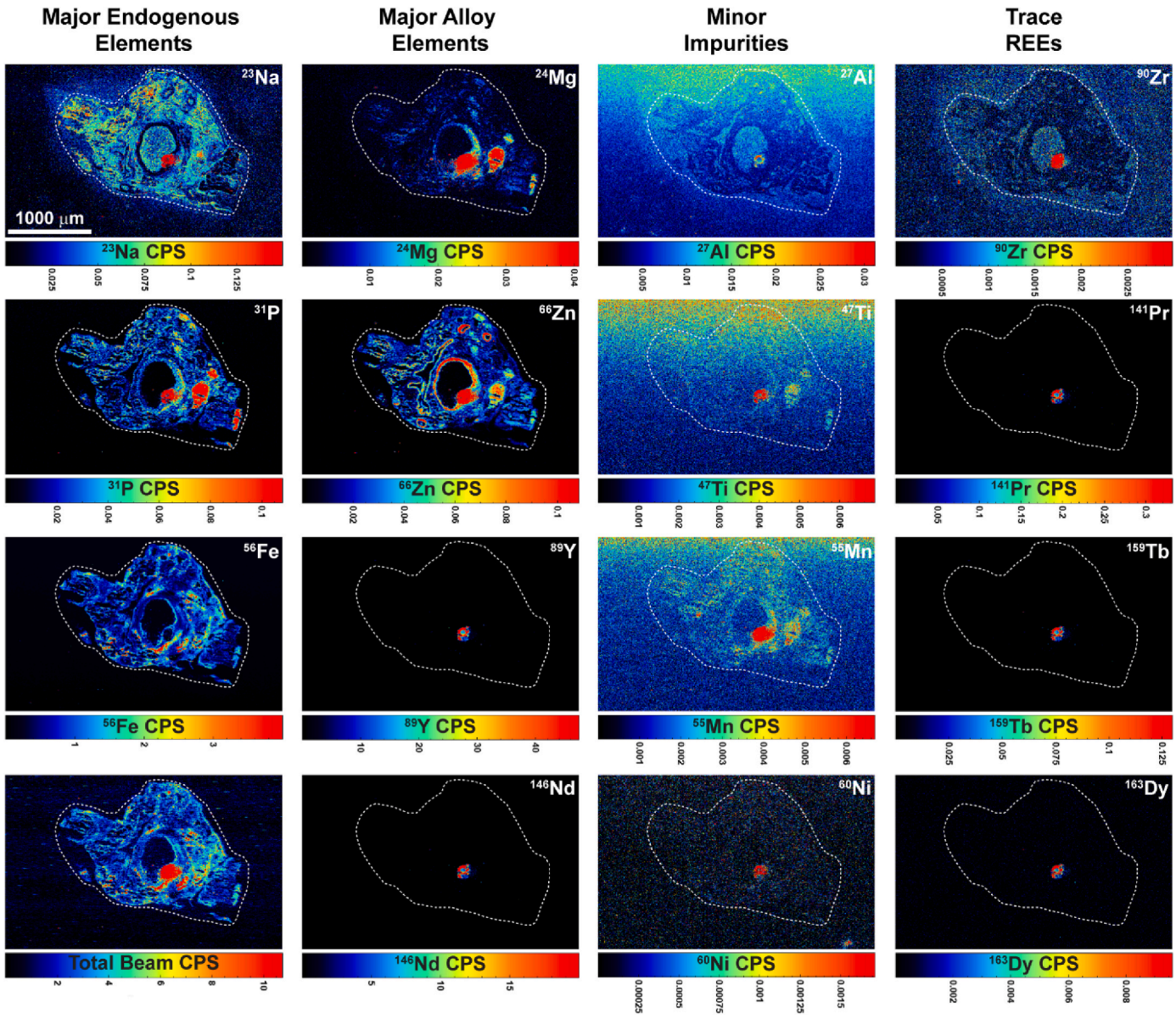

Fig. 3. LAM imaging and regional semi-quantitative analysis of major endogenous elements (^{23}Na, ^{31}P, and ^{56}Fe), major alloy elements (^{24}Mg, ^{66}Zn, ^{89}Y, and ^{146}Nd), minor impurities (^{27}Al, ^{47}Ti, ^{55}Mn, and ^{60}Ni), and examples of trace REEs (^{90}Zr, ^{141}Pr, ^{159}Tb, and ^{163}Dy) from 10 μm thick mouse aortic cross sections 30 d post implantation of WE22 wire. The maps presented in this figure consist of the upper 95 % of intensity values of all pixels presented for the respective element. The dashed white border is the demarcation of the whole tissue cross section for reference.

understand the spatial component of the clustering, regions were isolated and processed to delineate selected anatomic regions of the artery and implant (Fig. 4B and C). ^{89}Y and ^{143}Nd remain in the large REE cluster within the corroded wire implant and neointima regions. Within the adventitia, ^{89}Y and ^{143}Nd are less related and have reduced correlations when compared to the corrosion product, which was also confirmed by PCA analysis (**Supplement Figs. 5–7**).

It is noticed that REEs (highlighted by light salmon color) demonstrated high correlations (red blocks in the heap-map) and stayed together in the h-clustering dendrogram, while implant elements such as Mg, Mn, and Zn had higher correlation with ^{31}P and remained in proximity with each other. To understand the change of these relationships in different implanted tissue regions (illustrated in Fig. 4A, on the right), we applied this same analysis to more specific anatomical areas (Supplement Fig. 2); results clearly showed that in the vicinity of the implant, such as in the neointima tissues, REEs had higher correlation with each other and stayed closer in the h-clustering dendrogram. Specifically, the ^{89}Y channel was clustered closer to ^{143}Nd in neointimal areas (Fig. 4B) and shifted to other branches in adventitia tissues (Fig. 4C). These trends, the decrease of REEs' correlation and cluster dissociation of ^{89}Y and ^{143}Nd along the distance between the location of interest to the center of the implant, can be more clearly seen in the Supplement Fig. 2. More tissue scans were analyzed (Supplement Figs. 3–4), demonstrating a consistent trade-off. This pattern is further supported by the PCA analysis, where ^{89}Y and ^{143}Nd are in proximity to each other in the corrosion product region demonstrated in the biplot map, while ^{89}Y shift away from the ^{143}Nd cluster in adventitia regions (Supplementary Figs. 5–7).

3.2.3. *Implant derived ^{89}Y and ^{143}Nd*

As the relatedness of multiple REEs has been demonstrated by h-clustering and PCA, focus was placed on the most abundant REEs in WE22, Y and Nd. Fig. 5A demonstrates that when using the same cut-off values, ^{143}Nd (green) is closer to the wire origin when compared to ^{89}Y

Table 2
Minor impurity and trace elemental composition of WE22 wire characterized by ICP-QQQ-MS (unit = mass%).

Element	Sample 1	Sample 2	Sample 3	Average	Sd.
Al	0.0529	0.0155	0.0189	0.0291	0.0207
Ca	0.0252	0.0068	0.0141	0.0154	0.0092
Cr	0.0075	0.0062	0.0015	0.0051	0.0031
Mn	0.0554	0.0669	0.0272	0.0499	0.0204
Co	0.0007	0.0006	0.0005	0.0006	0.0001
Ni	0.0031	0.0021	0.0019	0.0024	0.0006
Ga	0.0309	0.0323	0.0288	0.0307	0.0018
Sr	0.0007	0.0005	0.0006	0.0006	0.0001
Ag	0.0021	0.0012	0.0005	0.0013	0.0008
Cd	0.0006	0.0005	0.0005	0.0005	0.0000
In	0.0005	0.0005	0.0005	0.0005	0.0000
Ba	0.0012	0.0010	0.0007	0.0010	0.0002
La	0.0001	0.0001	0.0001	0.0001	0.0000
Ce	0.0002	0.0001	0.0001	0.0001	0.0000
Eu	0.0000	0.0000	0.0000	0.0000	0.0000
Dy	0.0015	0.0016	0.0014	0.0015	0.0001
Tl	0.0005	0.0004	0.0004	0.0004	0.0000
Pb	0.0047	0.0047	0.0016	0.0037	0.0018
Bi	0.0008	0.0007	0.0007	0.0008	0.0001

(red) and nearly all ^{143}Nd signal is masked by the red ^{89}Y signal, indicating the colocalization of ^{89}Y and ^{143}Nd around the implant. Due to this variable relationship with respect to distance, the ^{89}Y and ^{143}Nd ratio in all different histological regions was explored (illustrated in Fig. 5B). ^{89}Y increased with the increase of ^{143}Nd signal across the whole tissue section (Fig. 5C), whereas ^{143}Nd and ^{31}P showed no such correlation (Supplement Fig. 8). When looking at the ^{89}Y-^{143}Nd distribution in Figs. 5C, ^{89}Y and ^{143}Nd appear to have higher correlations in areas closer to the implant (or areas that had high ^{89}Y+^{143}Nd signals) and lower correlations with an increased distance to the implant, which is supported by Spearman correlation coefficients ρ between ^{89}Y and ^{143}Nd, where a close to 1 ρ indicates positive correlation between ^{89}Y and ^{143}Nd strength and close to 0 ρ means poor correlation (Fig. 5E). When evaluating distance (e.g. adventitia regions yellow and blue in Figs. 5D), ^{89}Y+^{143}Nd total signal can vary over Log 3, clearly showing distance is not the mere determinant of ^{89}Y and ^{143}Nd signal strength. The nearby media and adventitia regions contained more total signal compared with areas farther away (Fig. 5D). There was a decrease in total signal of ^{89}Y+^{143}Nd as the distance from the wire origin increases (Fig. 5D), which is also associated with a reduction in the correlation coefficient calculated by Spearman's rank (Fig. 5E).

Regions with relatively high ^{89}Y and ^{143}Nd and small ^{89}Y/^{143}Nd variation were interrogated further. Plotting of ^{89}Y/^{143}Nd ratio over ^{89}Y+^{143}Nd signal and the pixel to wire center distances was performed (Fig. 6A and B). It is clear that the distribution of ^{89}Y/^{143}Nd ratio converged in areas closer to the implant or areas that had high ^{89}Y+^{143}Nd signal, while the distribution of ^{89}Y/^{143}Nd ratio spreads with an increased distance or decreased ^{89}Y+^{143}Nd signal. This trend was not shown over ^{31}P or ^{56}Fe signals (Fig. 6C and D). Instead, a seemingly more random distribution with high noise was observed. Note that, since the wire region (dark red) has low ^{56}Fe content and a wide range of ^{31}P signal, the region distinguished itself from other regions by showing a relatively converged ^{89}Y/^{143}Nd ratio (Fig. 6C and D).

^{56}Fe rich and ^{56}Fe low regions near the implant and in surrounding regions were evaluated for ^{89}Y and ^{143}Nd presence, using 99 % pixel cut-off values as a thresholded metric (Fig. 7). ^{56}Fe rich regions possessed highly correlated ^{89}Y/^{143}Nd ratios (Fig. 7B), with a significant reduction in the ^{56}Fe low regions. The ^{31}P signal was used to verify tissue/cellular presence, and evaluated both regions against their relative distance from the implant to demonstrate the distance effect on ^{89}Y/^{143}Nd ratios. High resolution scans (spot size 1 μm) of the H&E-stained sections demonstrate ^{56}Fe rich tissue regions are within the neointima and these regions correspond highly with F4/80+ MΦ's (Supplement Fig. 10), as well as ^{89}Y and ^{143}Nd (Fig. 7F–I). Two regions were selected from the adventitia layer, which had similar cell density (indicated by ^{31}P signal strength, Fig. 7A) and similar distances to the wire center (confirmed in Fig. 7B). Thus, the main difference is the ^{56}Fe signal strength. Strikingly, ^{89}Y/^{143}Nd ratio converged in the ^{56}Fe rich region and diverged in the ^{56}Fe low region independent of cell density (indicated by ^{31}P) and distance. The trend is further supported by the divergent Spearman correlation coefficients (Fig. 7B). To further confirm the results, additional samples were scanned with higher resolution (Fig. 7F–K). The localization of ^{56}Fe with ^{89}Y and ^{143}Nd as well as more specific ^{89}Y/^{143}Nd ratio in ^{56}Fe rich region indicates ^{89}Y and ^{143}Nd behavior is to some degree correlated with ^{56}Fe rich regions. In addition, when higher ^{89}Y/^{143}Nd correlation is observed in ^{56}Fe rich region, similar ^{31}P levels is detected in those areas, indicating it is more likely to be cell type, not cell number that regulates ^{89}Y and ^{143}Nd colocalization behaviors.

3.3. Semi-quantitative LAM

To understand metal concentrations in the tissue, tissue sections were scanned with gelatin standards spiked with elements of interest (0, 1, 5, 10, 20, and 50 ppm). Element concentrations were calculated using the data reduction scheme provided in iolite. The semi-quantitative scans are visualized in Fig. 8. Approximations of element concentration are shown in Supplement Fig. 9. Since normal physiological metal levels in the tissues can be several magnitudes lower than the levels caused by the implants, it is difficult to demonstrate the elemental ppm levels across the whole tissue section with a linear color scale. Therefore, the Log scale for ppm levels of pixels were plotted and arranged by regions (defined in Fig. 4A), so that the overall trend of metal level change was demonstrated quantitatively in Supplement Fig. 9B. Alloy elements such as ^{24}Mg, ^{89}Y, and ^{143}Nd remained high in the corroded products and decreased in the tissues. ^{24}Mg and ^{39}K demonstrated more uniform distribution in the tissues. For example, in the neointima, most ^{24}Mg signal is between 1000 and 10,000 PPM. However, ^{89}Y and ^{143}Nd, varies from 1 to 10,000 ppm in neointima. The result is consistent with prior reports where Y nanoparticles from Mg degradation elicit major variation of Y signal in the vicinity of implants [14]. We roughly estimated the concentration of elements in mM by assuming the tissue density is 1 g/mL. The dash-line axis on the right of each plot Supplement Fig. 9 represents the corresponding mM concentrations, and tabulated values can be found in Supplement Tables 4 and 5.

4. Discussion

A significant technical hurdle in the field of bioabsorbable metals is the lack of efficient and reliable methods to determine *in situ* elemental levels within tissue. Insightful attempts have been made to clarify the implant derived *in situ* elemental distribution, although most of the focus has been on orthopedic samples. Additionally, each elemental mapping technique for biological samples comes with their respective challenges regarding sample preparation, variable element sensitivity and specificity, and ease of data collection [33]. This study presents a state of the art mass spectrometry imaging approach to understand elemental distribution and semi-quantification in the WE22 wire implanted rodent aortic model [27]. An APOE−/− knockout transgenic mouse was used to simulate an atherosclerotic environment. Emphasis was placed on Y and Nd, two major alloying constituents in the WE22 alloy which are not endogenously present in the tissue.

4.1. Qualitative observations using LAM imaging

The *in vivo* corrosion products generated during biocorrosion of alloyed Mg can vary in presentation, and depends significantly on the alloy system used, the particular stage of corrosion evaluated, and microstructure [34,35]. The WE22 alloy described in this work was found to have significant degradation at 30 d implantation (Fig. 1), and produced a complex corrosion product consisting of Mg–Ca–P

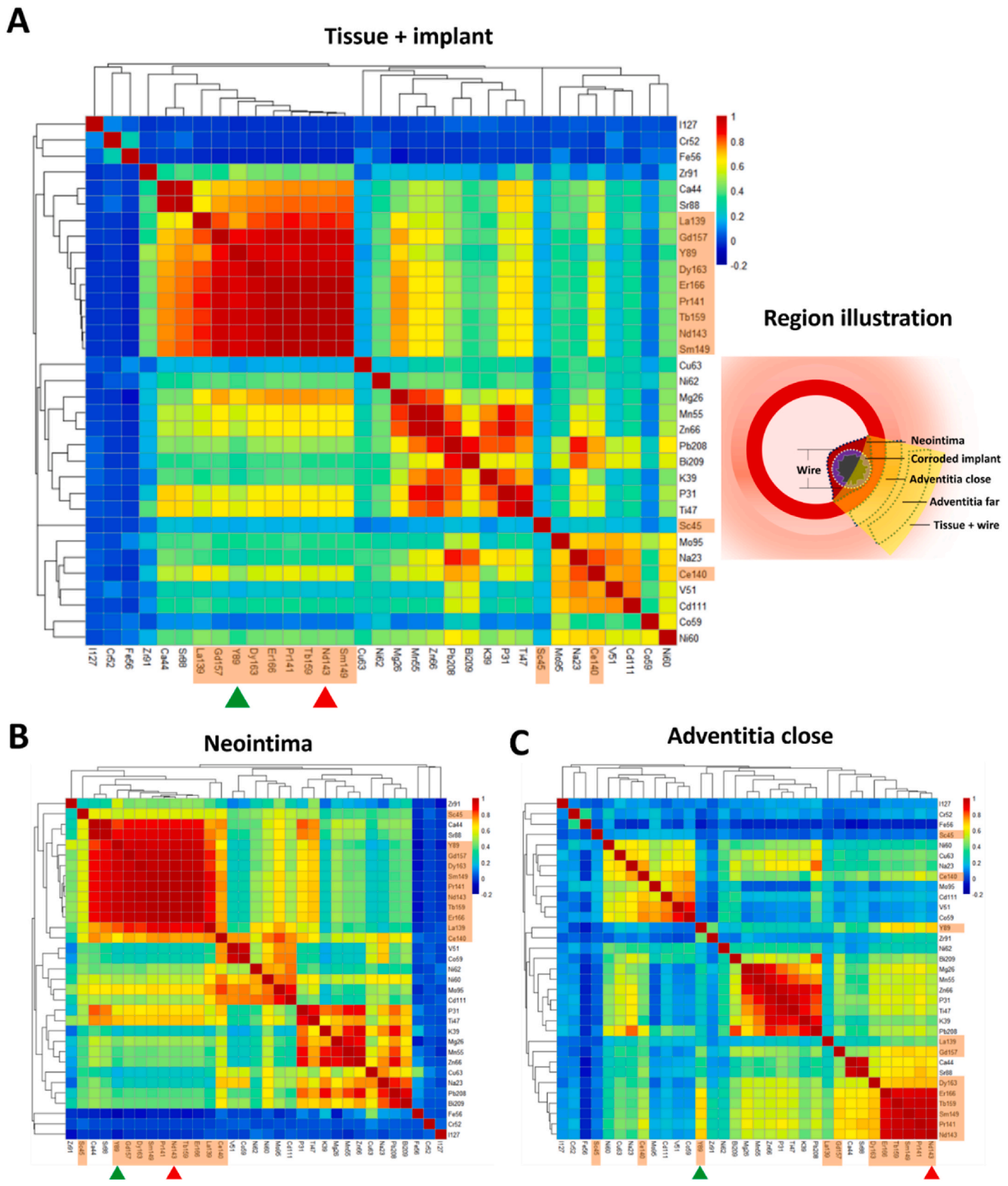

Fig. 4. Heatmap of correlations between different elements sorted according to h-clustering results of LAM data. Results were calculated and shown according to regions, such as tissue + implant or overall (A), neointima (B), and adventitia close to the implant (C). Definitions of different regions were demonstrated in the illustration next to the heat-map in Panel A. REEs are highlighted by the light salmon color in the heat-map labeling. ^{89}Y is indicated by the green arrows while ^{143}Nd channels are indicated by red arrows.

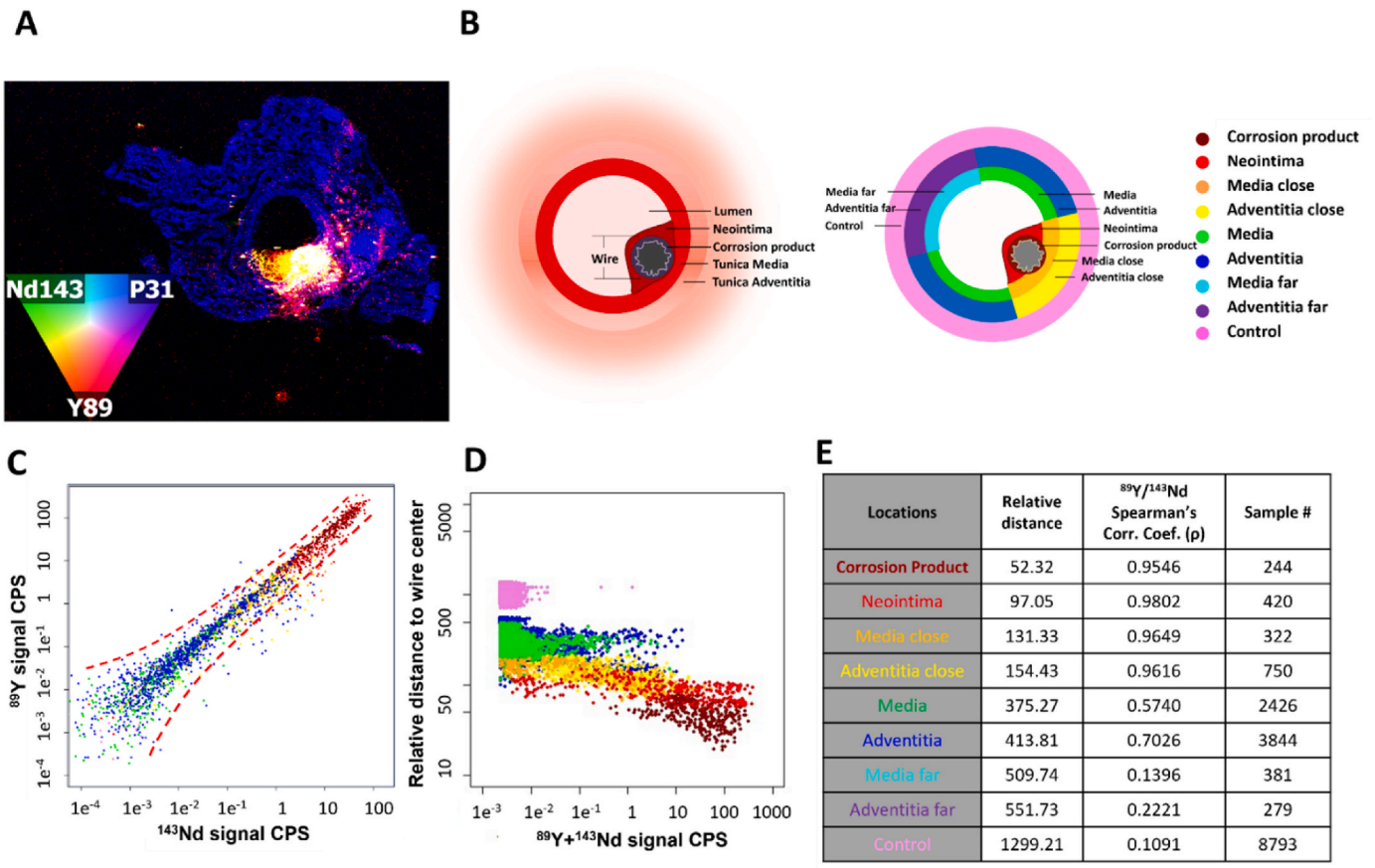

Locations	Relative distance	$^{89}Y/^{143}Nd$ Spearman's Corr. Coef. (ρ)	Sample #
Corrosion Product	52.32	0.9546	244
Neointima	97.05	0.9802	420
Media close	131.33	0.9649	322
Adventitia close	154.43	0.9616	750
Media	375.27	0.5740	2426
Adventitia	413.81	0.7026	3844
Media far	509.74	0.1396	381
Adventitia far	551.73	0.2221	279
Control	1299.21	0.1091	8793

Fig. 5. LAM of REEs and investigating ^{89}Y & ^{143}Nd relationships via individual pixel analysis of selected regions of interest. A co-localized RGB LAM map is shown from the same arterial cross section from Fig. 3 of a 30 d post implantation mouse aorta (A), where ^{89}Y (red), ^{143}Nd (green), and ^{31}P (blue) are overlayed and ^{89}Y and ^{143}Nd are colocalized and ^{31}P outlines tissue morphology. (B) Definition of different sub-tissue regions. (C) Investigation of the relationship of ^{89}Y and ^{143}Nd signals in the different sub tissue regions. (D) $^{89}Y+^{143}Nd$ signal strength versus traveling distance for the different tissue sub regions. (E) Spearman's correlation coefficient (ρ) where ρ decreases when Y diverges from Nd (all $p < 10^{-5}$).

containing phases, fine and variably sized REE bearing precipitates, and a mixed REE nano oxide substance (Fig. 2). Since the products from the WE22 material contained significant amounts Y and Nd as IMP's or $(Nd/Y)_2O_3$, efforts were focused to describe the presence for products of Y and Nd throughout the tissue sections. However, the *in situ* localization of other endogenous and alloy derived elements also display interesting patterns (Fig. 3). Qualitatively, ^{89}Y and ^{143}Nd presence and relatedness were not equivalent when distance, anatomical location, and correlation to other endogenous elements were considered (Figs. 4–7). This can be interpreted as inherent differences in the biodistribution and interaction of Y/Nd based products. An example of this can be observed in Fig. 4, where ^{89}Y is less related to the REE cluster in the adventitia. The adventitia appears to be the site of most ^{89}Y and ^{143}Nd variation, and the only anatomical location where ^{89}Y is seen largely without ^{143}Nd presence (Fig. 6). The observation of ^{89}Y rich products in the adventitia may suggest the preferential clearance of Y_2O_3, or Mg–Y phases over Nd_2O_3 or Mg-Nd-Y/Mg–Nd phases. Future studies should precisely clarify the composition and structure of REE containing phases/oxides which are differentially detected throughout the various tissue components (adventitia vs. media vs. neointima), as this was not the focus of the current study.

In comparison to the other arterial layers, the adventitia of arteries will experience large inflammatory cell recruitment after injurious events such as stent implantation or balloon angioplasty [36,37]. The adventitia is home to resident arterial MΦ's, which are able to respond rapidly to local stimuli and proliferate. Meanwhile, vasa vasorum supplies blood derived monocytes which can further differentiate into MΦ's locally [38]. The adventitial MΦ's have extensive contact with vascular lymphatic networks, where they can transport phagocytosed degradation products to local lymph nodes. After the initiation of corrosion, the inflammatory response is largely responsible for intereacting with metal remnants and corrosion products, which has been reported previously [25,35,39,40]. The MΦ's transport of degradation products towards draining lymphatics has been reported for bioabsorbable metals such as Fe scaffold as early as 2006 by Peuster [41], and recently for the iron bioresorbable coronary scaffold [42]. The lymphatic clearance pathway of insoluble products could be critical for bioabsorbable metal biocompatibility, but it remains understudied [43]. Importantly, multiple studies have demonstrated that MΦ's are capable of phagocytosing Mg based degradation products [22,23,40,44,45], potentially implicating MΦ's in the lymphatic clearance pathway for Mg material derived degradation products.

F4/80+ MΦ's were observed within the neointima and adventitia, and colocalized with ^{89}Y and ^{143}Nd signals from LAM imaging when serial sections were evaluated (Supplementary Fig. 10). Interestingly, these patterns appeared to coincide with total ^{56}Fe signal. Characterizing ^{56}Fe further as it relates to ^{89}Y and ^{143}Nd signal revealed striking relationships (Fig. 7). ^{56}Fe rich regions were correlated with a higher ratio and total amount of $^{89}Y/^{143}Nd$. It has been reported that MΦ's functions are closely related to systemic Fe regulation [46] and excess Fe storage as ferritin [47]. Additionally, MΦ's polarization is intricately linked to Fe regulated gene expression and overall Fe homeostasis [48–50]. Importantly, since WE22 and the degradation products contain low levels of Fe (Fig. 3, Table 1, Supplementary Fig. 9), the authors speculate that the majority of the ^{56}Fe signal observed is biologically derived, and fluctuations in ^{56}Fe signal could be caused by various

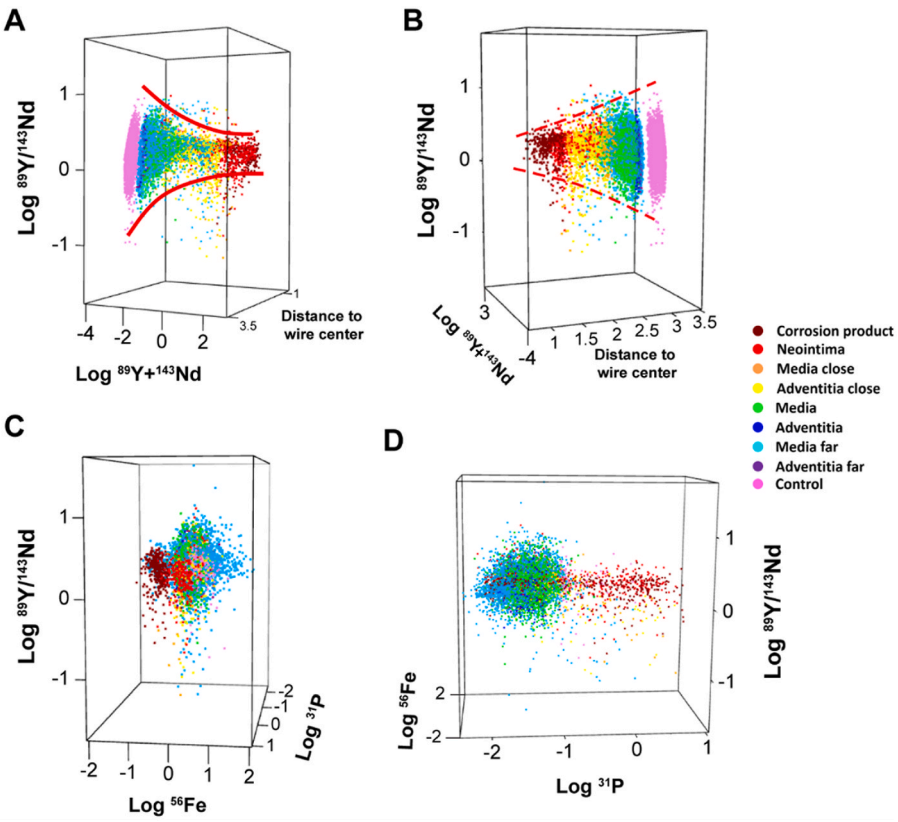

Fig. 6. 3D plots depicting the relationships of $^{89}Y/^{143}Nd$ ratio to different factors. (A) and (B) different views of 3D plot of (Y/Nd)-(Y + Nd)-Distance demonstrating that ^{89}Y and ^{143}Nd ratios are dependent on ^{89}Y and ^{143}Nd signal strength (characterized as the Y + Nd signal) and the distances from the pixel to the wire center. The ratio of ^{89}Y and ^{143}Nd signals (shown as Y/Nd) distributions demonstrated trumpet-like pattern in A and B. (C) and (D) different views of 3D plot of (Y/Nd)-Fe-P demonstrating more random distribution patterns of Y/Nd ratio to ^{56}Fe, as well as ^{31}P. Sample size, see Fig. 5E.

polarized MΦ's populations. Future studies could utilize techniques such as rare earth isotope tagged antibody labeling, to allow for a robust concurrent phenotypic description of Fe rich cells using LAM as described in other studies [51].

Proper tissue regeneration within the original footprint of the stent strut is critical to fully resolve the inflammatory reaction, and regeneration should follow corrosion product removal. MΦ's must infiltrate the product in order to initiate the regenerative response, which would be followed by other tissue depositing cells [52]. It has been shown that tissue infiltration can occur for certain Mg materials, such as the Mg–Dy based alloy system Resoloy [53]. We observed suspected tissue deposition within the original footprint of the wire upon inspection with SEM-BSE (Supplement Fig. 11), which corroborates that transport of product out of the original implant footprint likely occurs.

4.2. Semi-quantitative LAM analysis

It is challenging to determine *in vivo* concentration of corrosion products. Currently, the best estimations rely on collecting tissue or fluid directly from the implant site and performing elemental analysis, although this approach cannot capture spatial information [54]. To the authors knowledge, this study for the first time reports relative estimations of the concentrations of Mg, and REE's near the interface and in the adjacent tissue surrounding a Mg arterial implant with the spatial origin of the measurements conserved (Fig. 8A and B). Since the mass spectrometry data is measured on a per pixel basis, it is more representative to visualize the distribution of all mass spectra (pixels) collected.

The concentrations for pixels vary by many orders of magnitude, which significantly skews interpretation of an average pixel value. Therefore, the median value of all pixels within the regions is presented (Supplement Tables 4 and 5). The largest relative Mg concentration originates at the wire, with a decreasing gradient away from the tissue material interface. The pixels identified within the neointima region possess a median concentration of 2752 ppm (114.6 mM) for Mg. It should be noted that Mg is endogenously present throughout the tissue, and LAM measurements cannot distinguish the origin due to overlapping presence of biological Mg isotopes with implant derived isotopes.

To relate the findings of this study to previous *in vitro* biocompatibility investigations requires some assumptions. In vitro biocompatibility studies usually test Mg^{2+} in solution, using dissolved metal salts. If it is assumed that a moderate fraction of the measured concentration in each pixel was soluble when close to the implant (30–50 %), more than half of the pixels within the neointima may remain at or above what is reported as safe *in vitro* for Mg [54,55] (approximately 10 mM for L929 cells, 30 mM for RAW 264.7). In the adventitial compartments, median values of Mg are approximated at 1336 ppm–828 ppm (55.7–34.5 mM), which are closer to more tolerable Mg concentrations. It has been reported that some cell lines *in vitro*, such as HUCPV cells, are highly tolerant to supraphysiological Mg concentrations (LD_{50} 73 mM) [11]. Importantly, the pixels which have the highest values of Mg are near the interface of the material. Upon closer inspection of the interface, viable F4/80 + MΦ's (Supplement Fig. 10) are present. Previous work has shown *in vitro* that degrading Mg discs are correlated with a highly viable sub population of co-cultured inflammatory MΦ's, which are able to survive at high Mg concentrations [55]. The proportion of Mg in various bound and free forms near the bioimplant interface is complex and dynamic [56]. The local microenvironment created by inflammatory MΦ's modulates the pH and secreted extracellular protein profile, which can ultimately alter the stability of initial corrosion products ($MgO/Mg(OH)_2$), and degree of metal chelation by proteins [55–57]. To further complicate the matter, phagocytosed Mg based corrosion

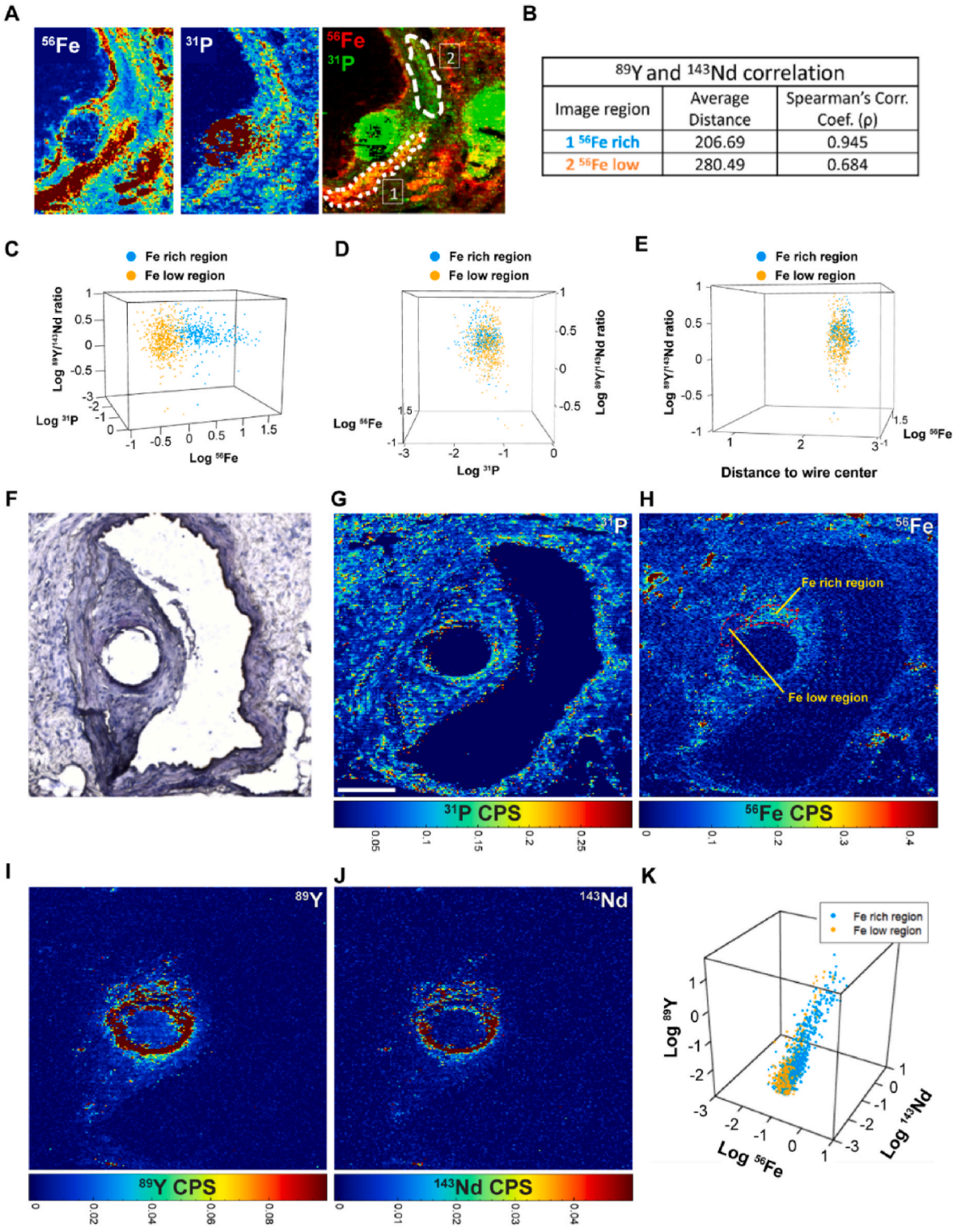

Fig. 7. ^{89}Y and ^{143}Nd ratios are highly dependent on the ^{56}Fe signal in adventitia. (A) Two distinct regions observed in adventitia, Fe-rich and Fe-low regions. Both regions contain a similar level of ^{31}P, indicating the two regions have similar cell density. (B) ^{89}Y-^{143}Nd correlations indicated by Spearman correlation coefficients are significantly different in different regions ($p < 10^{-10}$) (sample size: Fe-rich n = 356, Fe-low n = 502). (C) 3D-plot of (Y/Nd)-Fe-P, showing diverged ^{56}Fe levels correlates with the diverged ^{89}Y/^{143}Nd distribution patterns, (D and E) 3D-plots showing ^{31}P level and distance have minimum effects on Y/Nd ratio. (F) Hematoxylin stain of an implanted site. (G–J) The corresponding high resolution LAM on the neighboring tissue in Panel F. (K) 3D Plot shows that higher ^{56}Fe level corresponds with higher ^{89}Y as well as higher ^{143}Nd signal, (sample size: Fe-rich n = 633, Fe-low n = 532).

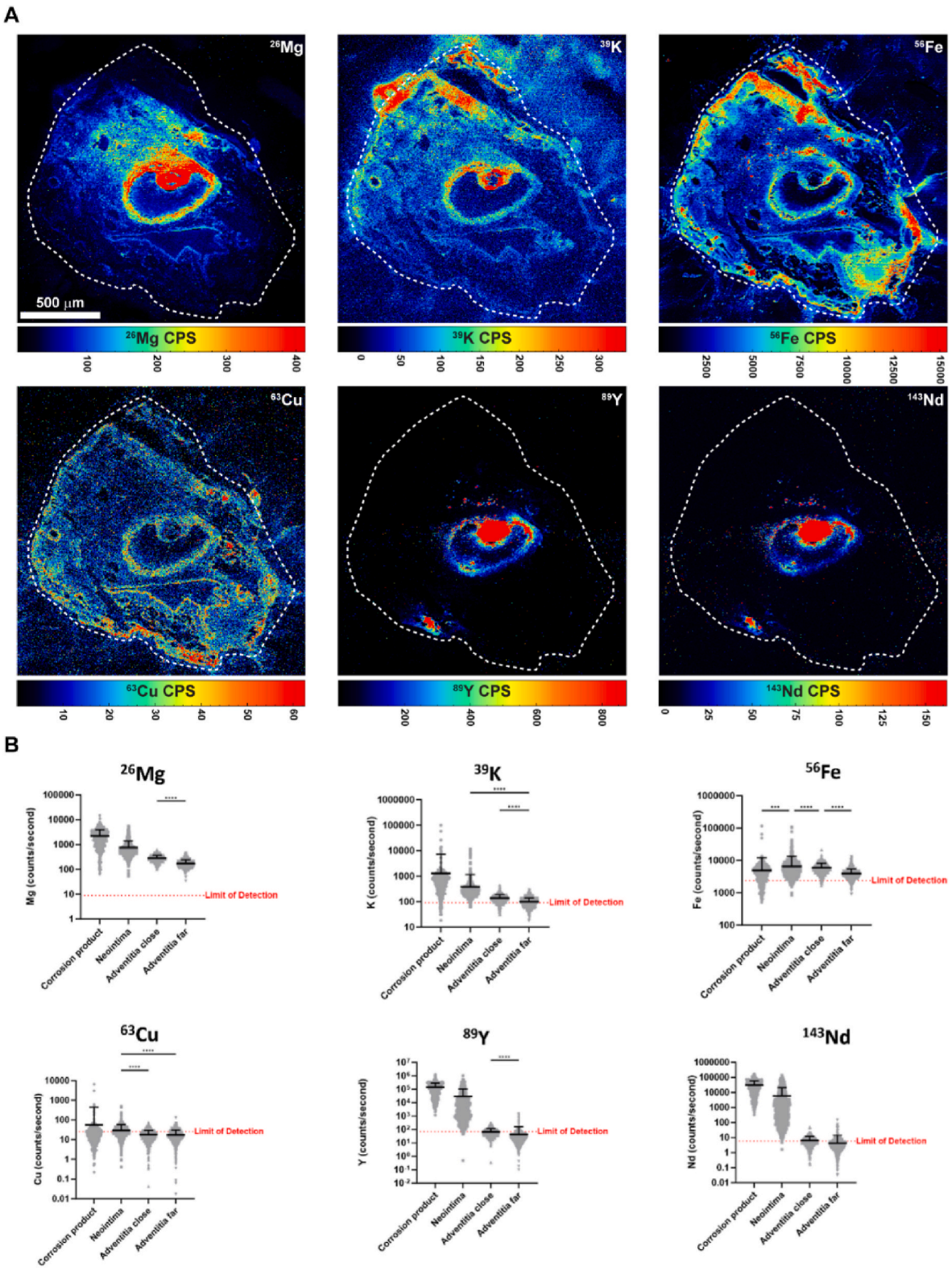

Fig. 8. Semi-quantitative analysis of alloy related elements of LAM images of mouse abdominal aorta cross sections 30-day post implantation of WE22 wire. (A) Mapping of metallic elements. (B) Dot plot showing raw data extracted from each mass spectrum (pixel) and plotted according to specific sub tissue regions. Region sample sizes (# of pixels) are as follows: Corrosion product (n = 364), Neointima (n = 882), Adventitia close (n = 448), Adventitia far (n = 612).

products could experience further digestion within phagolysosomes [40], which should increase intracellular Mg^{2+} and ultimately force MΦ's to transport excess Mg^{2+} into the extracellular space through established mechanisms [58], increasing extracellular Mg^{2+}. Ultimately, determining whether the total Mg concentration detected in LAM scans is comparable to *in vitro* studies which use Mg^{2+} is convoluted by these factors, since the amount of extracellular Mg^{2+} local to the implant *in vivo* is not known.

The interpretation for Y and Nd approximation is slightly more straightforward since they are not endogenously present in the tissue. In

the neointima, the median concentration for Y was 64 ppm and 73 ppm for Nd (0.71 mM, and 0.51 mM respectively). Both values are below the reported LD_{50} values for Y and Nd chloride exposure to RAW 264.7 cells [11]. Interestingly, the concentration values starkly drop-off in terms of magnitude when evaluating the adventitia. Many pixels in the adventitial regions are above the LOD for Y, and not above the LOD for Nd. The results suggest that proportionally less Nd is present further from the implant interface, confirming findings in Figs. 4 and 5, that Nd based products may be less preferential to transport compared with Y. Although prior studies evaluated salts of Y and Nd, our study found that a significant amount of Y and Nd were present as nano oxides and IMP's (Fig. 2). There has been some biotoxicity work performed on $(Nd,Y)_2O_3$ nano oxides, although the lack of direct Y/Nd comparison and differences in concentrations limits the interpretation of these works in the context of this study [59,60]. It is currently unknown why Nd is less efficient in being transported compared to Y. It may be inferred that the increased relative toxicity of Nd compared to Y plays a role [11].

4.3. Limitations

Although high estimations of Mg, Y, and Nd are given, a limitation of the analysis is the lack of metal speciation determination. Metallic particles cannot be distinguished from oxides, soluble forms of each element, or bound to proteins, which all possess different biocompatibility thresholds. Therefore, the above-mentioned values can be interpreted variably if different proportions of potential byproducts are considered. Furthermore, even if techniques that can discern metal speciation are used, sample preparation would have to be tightly controlled in order to prevent inadvertent precipitation of ions. Additionally, it is not possible to discern biological vs. implant derived endogenous elements such as Fe or Mg due to the isotope similarity within the implants and tissue. In the future, co-registration of LAM scans with techniques that can provide semi-quantitative elemental species information would improve conclusions drawn from this technique [33]. This limits the interpretation of the concentration values in terms of toxicity since the oxidation state of the reported metals is key in understanding their toxicological implications, as well as the origin of Fe and Mg (implant vs. biological) throughout tissue sections. Finally, preparation artifacts such as sectioning and handling could inadvertently change the total amount of elements present.

Our estimations must also be contextualized with the degree of corrosion of the WE22 wire. The material analyzed at 30-day via BSE and EDX indicates near full conversion of the metallic material into corrosion products (Fig. 1) in some metallographic sections. Current on market and next generation Mg scaffolds can maintain metallic cross sections for more than 2 months [61], which would in turn decrease the overall amount of liberated Mg and REEs measured in neighboring tissues. The values measured in this study may represent concentrations caused by rapid bioabsorbtion of Mg, which is occasionally seen in the clinic [62,63]. It is feasible that our APOE−/− model accelerated the bioabsorbtion of the WE22 material, due to its documented increase in local inflammation [19], and the recent relationship demonstrated between increased local inflammation and increased local Mg stent corrosion [64]. Future work should precisely measure a time series of Mg implants, with a range of corrosion rates to determine concentrations of corrosion products more accurately in neighboring tissue.

5. Conclusions

This study demonstrates how a state-of-the-art imaging method (LA-ICP-TOF-MS, or laser ablation mapping, LAM) can provide *in situ* qualitative and semi-quantitative description of the soft tissue elemental distribution surrounding a bioabsorbable Mg vascular implant. Here, it is shown that

1. The corrosion byproducts of a rare earth containing Mg implant are complex and possess REE based oxides and secondary phases.
2. Using the distribution of $^{89}Y/^{143}Nd$ ratio as a corrosion product indicator, REE based corrosion products are variable as a function of location, and distance from implant.
3. ^{89}Y is able to diffuse through the vascular tissue more readily than ^{143}Nd.
4. Endogenous Fe levels correspond with $^{89}Y/^{143}Nd$ ratio changes, which is potentially influenced by the presence of MΦ's.
5. When estimating pixels from the tissue neighboring the implant (neointima), median values for all species of Mg were approximated at 2752 ppm, with the pixels containing the most Mg situated at the interface.
6. When estimating all pixels from the adventitial tissue near and far from the implant, median values of all species of Mg were approximated between 1336 ppm and 828 ppm.
7. Pixels measured in the neointima of the implant for all species of Y and Nd showed median values of 64 ppm and 73 ppm respectively.

Ethics approval and consent to participate

Our study employs the use of rodents, which was approved by the animal care and Use committee of Michigan Technological University. No human subjects were involved.

CRediT authorship contribution statement

Weilue He: Writing – review & editing, Writing – original draft, Methodology, Investigation, Formal analysis, Data curation, Conceptualization. **Keith W. MacRenaris:** Writing – review & editing, Writing – original draft, Methodology, Investigation, Formal analysis, Data curation, Conceptualization. **Adam Griebel:** Writing – review & editing, Validation, Resources, Investigation, Conceptualization. **Maria P. Kwesiga:** Writing – review & editing, Investigation, Data curation, Conceptualization. **Erico Freitas:** Writing – review & editing, Formal analysis, Data curation, Conceptualization. **Amani Gillette:** Writing – review & editing, Visualization, Methodology, Formal analysis. **Jeremy Schaffer:** Writing – review & editing, Resources, Investigation. **Thomas V. O'Halloran:** Writing – review & editing, Writing – original draft, Supervision, Resources, Investigation, Funding acquisition, Conceptualization. **Roger J. Guillory II:** Writing – review & editing, Writing – original draft, Supervision, Investigation, Funding acquisition, Formal analysis, Conceptualization.

Declaration of competing interest

Adam Griebel and Jeremy Schaffer are currently employed by Fort Wayne Metals. There are no conflicts of interest to report.

Acknowlegdments

This research was carried out in collaboration with the Quantitative Bio Element Analysis and Mapping (QBEAM) Center at Michigan State University and The National Research Resource for Quantitative Elemental Mapping for the Life Sciences (QE-Map) under Grant P41 GM135018 (as well as Grant S10OD026786) from the National Institute of General Medical Sciences of the National Institutes of Health. This work was partially supported by the National Heart Blood Lung Institute under the award numbers R15HL167221-01 and R15HL167221-02 (RJG).

Appendix A. Supplementary data

Supplementary data to this article can be found online at https://doi.org/10.1016/j.bioactmat.2024.07.023.

References

[1] C. Li, C. Guo, V. Fitzpatrick, A. Ibrahim, M.J. Zwierstra, P. Hanna, A. Lechtig, A. Nazarian, S.J. Lin, D.L. Kaplan, Design of biodegradable, implantable devices towards clinical translation, Nat. Rev. Mater. 5 (1) (2020) 61–81.

[2] R. Kulkarni, K. Pani, C. Neuman, F. Leonard, Polylactic acid for surgical implants, Arch. Surg. 93 (5) (1966) 839–843.

[3] Y.F. Zheng, X.N. Gu, F. Witte, Biodegradable metals, Mater. Sci. Eng. R Rep. 77 (2014) 1–34.

[4] A.A. Oliver, M. Sikora-Jasinska, A.G. Demir, R.J. Guillory II, Recent advances and directions in the development of bioresorbable metallic cardiovascular stents: insights from recent human and in vivo studies, Acta Biomater. 127 (2021) 1–23.

[5] S. Verheye, A. Wlodarczak, P. Montorsi, J. Torzewski, J. Bennett, M. Haude, G. Starmer, T. Buck, M. Wiemer, A.A. Nuruddin, BIOSOLVE-IV-registry: safety and performance of the Magmaris scaffold: 12-month outcomes of the first cohort of 1,075 patients, Cathet. Cardiovasc. Interv. 98 (1) (2021) E1–E8.

[6] H. Hermawan, D. Dubé, D. Mantovani, Developments in metallic biodegradable stents, Acta Biomater. 6 (5) (2010) 1693–1697.

[7] H. Li, P. Wang, G. Lin, J. Huang, The role of rare earth elements in biodegradable metals: a review, Acta Biomater. 129 (2021) 33–42.

[8] E. Willbold, X. Gu, D. Albert, K. Kalla, K. Bobe, M. Brauneis, C. Janning, J. Nellesen, W. Czayka, W. Tillmann, Effect of the addition of low rare earth elements (lanthanum, neodymium, cerium) on the biodegradation and biocompatibility of magnesium, Acta Biomater. 11 (2015) 554–562.

[9] Y. Ding, C. Wen, P. Hodgson, Y. Li, Effects of alloying elements on the corrosion behavior and biocompatibility of biodegradable magnesium alloys: a review, J. Mater. Chem. B 2 (14) (2014) 1912–1933.

[10] F. Witte, N. Hort, C. Vogt, S. Cohen, K.U. Kainer, R. Willumeit, F. Feyerabend, Degradable biomaterials based on magnesium corrosion, Curr. Opin. Solid State Mater. Sci. 12 (5–6) (2008) 63–72.

[11] F. Feyerabend, J. Fischer, J. Holtz, F. Witte, R. Willumeit, H. Drücker, C. Vogt, N. Hort, Evaluation of short-term effects of rare earth and other elements used in magnesium alloys on primary cells and cell lines, Acta Biomater. 6 (5) (2010) 1834–1842.

[12] A. Drynda, N. Deinet, N. Braun, M. Peuster, Rare earth metals used in biodegradable magnesium-based stents do not interfere with proliferation of smooth muscle cells but do induce the upregulation of inflammatory genes, J. Biomed. Mater. Res. Part A: An Official Journal of The Society for Biomaterials, The Japanese Society for Biomaterials, and The Australian Society for Biomaterials and the Korean Society for Biomaterials 91 (2) (2009) 360–369.

[13] A. Turyanskaya, M. Rauwolf, T.A. Grünewald, M. Meischel, S. Stanzl-Tschegg, J. F. Löffler, P. Wobrauschek, A.M. Weinberg, H.C. Lichtenegger, C. Streli, μXRF elemental mapping of bioresorbable magnesium-based implants in bone, Materials 9 (10) (2016) 811.

[14] F. Amerstorfer, S.F. Fischerauer, L. Fischer, J. Eichler, J. Draxler, A. Zitek, M. Meischel, E. Martinelli, T. Kraus, S. Hann, Long-term in vivo degradation behavior and near-implant distribution of resorbed elements for magnesium alloys WZ21 and ZX50, Acta Biomater. 42 (2016) 440–450.

[15] N. Peruzzi, S. Galli, H. Helmholz, N. Kardjilov, D. Krüger, H. Markötter, J. Moosmann, D. Orlov, Z. Prgomet, R. Willumeit-Römer, Multimodal ex vivo methods reveal that Gd-rich corrosion byproducts remain at the implant site of biodegradable Mg-Gd screws, Acta Biomater. 136 (2021) 582–591.

[16] A.P. Morrell, H. Floyd, J.F.W. Mosselmans, L.M. Grover, H. Castillo-Michel, E. T. Davis, J.E. Parker, R.A. Martin, O. Addison, Improving our understanding of metal implant failures: multiscale chemical imaging of exogenous metals in ex-vivo biological tissues, Acta Biomater. 98 (2019) 284–293.

[17] S. Gruhl, F. Witte, J. Vogt, C. Vogt, Determination of concentration gradients in bone tissue generated by a biologically degradable magnesium implant, J. Anal. Atomic Spectrom. 24 (2) (2009) 181–188.

[18] J. Draxler, A. Zitek, M. Meischel, S.E. Stranzl-Tschegg, B. Mingler, E. Martinelli, A. M. Weinberg, T. Prohaska, Regionalized quantitative LA-ICP-MS imaging of the biodegradation of magnesium alloys in bone tissue, J. Anal. Atomic Spectrom. 30 (12) (2015) 2459–2468.

[19] L.M. Morath, R.J. Guillory, A.A. Oliver, S.Q. Liu, M.L. Bocks, G.K. Levy, J. W. Drelich, J. Goldman, Conventional platinum metal implants provoke restenosis responses in atherogenic but not healthy arteries, Science 5 (2) (2023) 25.

[20] K.S. Meir, E. Leitersdorf, Atherosclerosis in the apolipoprotein E–deficient mouse: a decade of progress, Arterioscler. Thromb. Vasc. Biol. 24 (6) (2004) 1006–1014.

[21] M. Costantino, A. Schuster, H. Helmholz, A. Meyer-Rachner, R. Willumeit-Römer, B. Luthringer-Feyerabend, Inflammatory response to magnesium-based biodegradable implant materials, Acta Biomater. 101 (2020) 598–608.

[22] L. Jin, C. Chen, G. Jia, Y. Li, J. Zhang, H. Huang, B. Kang, G. Yuan, H. Zeng, T. Chen, The bioeffects of degradable products derived from a biodegradable Mg-based alloy in macrophages via heterophagy, Acta Biomater. 106 (2020) 428–438.

[23] L. Jin, C. Chen, Y. Li, F. Yuan, R. Gong, J. Wu, H. Zhang, B. Kang, G. Yuan, H. Zeng, A biodegradable Mg-based alloy inhibited the inflammatory response of THP-1 cell-derived macrophages through the TRPM7–PI3K–AKT1 signaling axis, Front. Immunol. 10 (2019) 2798.

[24] A.-M. Negrescu, M.-G. Necula, A. Gebaur, F. Golgovici, C. Nica, F. Curti, H. Iovu, M. Costache, A. Cimpean, In Vitro macrophage immunomodulation by poly (ε-caprolactone) based-coated AZ31 Mg alloy, Int. J. Mol. Sci. 22 (2) (2021) 909.

[25] F. Witte, H. Ulrich, M. Rudert, E. Willbold, Biodegradable magnesium scaffolds: Part 1: appropriate inflammatory response, J. Biomed. Mater. Res. 81 (3) (2007) 748–756.

[26] A.J. Griebel, J.E. Schaffer, T.M. Hopkins, A. Alghalayini, T. Mkorombindo, K. O. Ojo, Z. Xu, K.J. Little, S.K. Pixley, An in vitro and in vivo characterization of fine WE43B magnesium wire with varied thermomechanical processing conditions, J. Biomed. Mater. Res. B Appl. Biomater. 106 (5) (2018) 1987–1997.

[27] D. Pierson, J. Edick, A. Tauscher, E. Pokorney, P. Bowen, J. Gelbaugh, J. Stinson, H. Getty, C.H. Lee, J. Drelich, A simplified in vivo approach for evaluating the bioabsorbable behavior of candidate stent materials, J. Biomed. Mater. Res. B Appl. Biomater. 100 (1) (2012) 58–67.

[28] R.J. Guillory, A.A. Oliver, E.K. Davis, E.J. Earley, J.W. Drelich, J. Goldman, Preclinical in vivo evaluation and screening of zinc-based degradable metals for endovascular stents, Jom 71 (2019) 1436–1446.

[29] S. Leleu, B. Rives, J. Bour, N. Causse, N. Pébère, On the stability of the oxides film formed on a magnesium alloy containing rare-earth elements, Electrochim. Acta 290 (2018) 586–594.

[30] J. Liu, D. Bian, Y. Zheng, X. Chu, Y. Lin, M. Wang, Z. Lin, M. Li, Y. Zhang, S. Guan, Comparative in vitro study on binary Mg-RE (Sc, Y, La, Ce, Pr, Nd, Sm, Eu, Gd, Tb, Dy, Ho, Er, Tm, Yb and Lu) alloy systems, Acta Biomater. 102 (2020) 508–528.

[31] L. Yang, N. Hort, D. Laipple, D. Höche, Y. Huang, K.U. Kainer, R. Willumeit, F. Feyerabend, Element distribution in the corrosion layer and cytotoxicity of alloy Mg–10Dy during in vitro biodegradation, Acta Biomater. 9 (10) (2013) 8475–8487.

[32] C.-H. Shih, C.-Y. Huang, T.-H. Hsiao, C.-S. Lin, The effect of the secondary phases on the corrosion of AZ31B and WE43-T5 Mg alloys, Corrosion Sci. 211 (2023) 110920.

[33] D.Z. Zee, K.W. MacRenaris, T.V. O'Halloran, Quantitative imaging approaches to understanding biological processing of metal ions, Curr. Opin. Chem. Biol. 69 (2022) 102152.

[34] G. Song, A. Atrens, Understanding magnesium corrosion—a framework for improved alloy performance, Adv. Eng. Mater. 5 (12) (2003) 837–858.

[35] J. Zhang, H. Li, W. Wang, H. Huang, J. Pei, H. Qu, G. Yuan, Y. Li, The degradation and transport mechanism of a Mg-Nd-Zn-Zr stent in rabbit common carotid artery: a 20-month study, Acta Biomater. 69 (2018) 372–384.

[36] E.-i. Okamoto, T. Couse, H. De Leon, J. Vinten-Johansen, R.B. Goodman, N. A. Scott, J.N. Wilcox, Perivascular inflammation after balloon angioplasty of porcine coronary arteries, Circulation 104 (18) (2001) 2228–2235.

[37] P. Libby, G.K. Hansson, Inflammation and immunity in diseases of the arterial tree: players and layers, Circ. Res. 116 (2) (2015) 307–311.

[38] L. Honold, M. Nahrendorf, Resident and monocyte-derived macrophages in cardiovascular disease, Circ. Res. 122 (1) (2018) 113–127.

[39] J. Zhang, S. Hiromoto, T. Yamazaki, J. Niu, H. Huang, G. Jia, H. Li, W. Ding, G. Yuan, Effect of macrophages on in vitro corrosion behavior of magnesium alloy, J. Biomed. Mater. Res. 104 (10) (2016) 2476–2487.

[40] L. Dong, Z. Shen, H. Zhang, B. Zhang, Y. Zhou, X. Lv, X. Hong, J. Liu, W. Yang, Effect of unsoluble corrosion products of WE43 alloys in vitro on macrophages, J. Biomed. Mater. Res. Part A 112 (1) (2024) 6–19.

[41] M. Peuster, C. Hesse, T. Schloo, C. Fink, P. Beerbaum, C. von Schnakenburg, Long-term biocompatibility of a corrodible peripheral iron stent in the porcine descending aorta, Biomaterials 27 (28) (2006) 4955–4962.

[42] J.-F. Zheng, Z.-W. Xi, Y. Li, J.-N. Li, H. Qiu, X.-Y. Hu, T. Luo, C. Wu, X. Wang, L.-F. Song, Long-term safety and absorption assessment of a novel bioresorbable nitrided iron scaffold in porcine coronary artery, Bioact. Mater. 17 (2022) 496–505.

[43] J.W. Drelich, J. Goldman, Bioresorbable vascular metallic scaffolds: current status and research trends, Curr. Opin. Biomed. Eng. 24 (2022) 100411.

[44] J. Zhang, S. Hiromoto, T. Yamazaki, H. Huang, G. Jia, H. Li, G. Yuan, Macrophage phagocytosis of biomedical Mg alloy degradation products prepared by electrochemical method, Mater. Sci. Eng. C 75 (2017) 1178–1183.

[45] C. Liu, P. He, P. Wan, M. Li, K. Wang, L. Tan, Y. Zhang, K. Yang, The in vitro biocompatibility and macrophage phagocytosis of Mg17Al12 phase in Mg–Al–Zn alloys, J. Biomed. Mater. Res. 103 (7) (2015) 2405–2415.

[46] N. Sukhbaatar, T. Weichhart, Iron regulation: macrophages in control, Pharmaceuticals 11 (4) (2018) 137.

[47] P. Arosio, R. Ingrassia, P. Cavadini, Ferritins: a family of molecules for iron storage, antioxidation and more, Biochim. Biophys. Acta Gen. Subj. 1790 (7) (2009) 589–599.

[48] M. Jung, C. Mertens, B. Brüne, Macrophage iron homeostasis and polarization in the context of cancer, Immunobiology 220 (2) (2015) 295–304.

[49] N.C. Winn, K.M. Volk, A.H. Hasty, Regulation of tissue iron homeostasis: the macrophage "ferrostat", JCI insight 5 (2) (2020).

[50] G. Cairo, S. Recalcati, A. Mantovani, M. Locati, Iron trafficking and metabolism in macrophages: contribution to the polarized phenotype, Trends Immunol. 32 (6) (2011) 241–247.

[51] B. Neumann, S. Hösl, K. Schwab, F. Theuring, N. Jakubowski, Multiplex LA-ICP-MS bio-imaging of brain tissue of a parkinsonian mouse model stained with metal-coded affinity-tagged antibodies and coated with indium-spiked commercial inks as internal standards, J. Neurosci. Methods 334 (2020) 108591.

[52] A.K. Gaharwar, I. Singh, A. Khademhosseini, Engineered biomaterials for in situ tissue regeneration, Nat. Rev. Mater. 5 (9) (2020) 686–705.

[53] R. Menze, E. Wittchow, In vitro and in vivo evaluation of a novel bioresorbable magnesium scaffold with different surface modifications, J. Biomed. Mater. Res. B Appl. Biomater. 109 (9) (2021) 1292–1302.

[54] J. Wang, F. Witte, T. Xi, Y. Zheng, K. Yang, Y. Yang, D. Zhao, J. Meng, Y. Li, W. Li, Recommendation for modifying current cytotoxicity testing standards for biodegradable magnesium-based materials, Acta Biomater. 21 (2015) 237–249.

[55] M.P. Kwesiga, A.A. Gillette, F. Razaviamri, M.E. Plank, A.L. Canull, Z. Alesch, W. He, B.P. Lee, R.J. Guillory II, Biodegradable magnesium materials regulate ROS-RNS balance in pro-inflammatory macrophage environment, Bioact. Mater. 23 (2023) 261–273.

[56] R. Willumeit-Römer, The interface between degradable Mg and tissue, Jom 71 (4) (2019) 1447–1455.
[57] Z. Mardina, J. Venezuela, M.S. Dargusch, Z. Shi, A. Atrens, The influence of the protein bovine serum albumin (BSA) on the corrosion of Mg, Zn, and Fe in Zahrina's simulated interstitial fluid, Corrosion Sci. 199 (2022) 110160.
[58] A.M. Romani, Cellular magnesium homeostasis, Arch. Biochem. Biophys. 512 (1) (2011) 1–23.
[59] Y. Chen, L. Yang, C. Feng, L.-P. Wen, Nano neodymium oxide induces massive vacuolization and autophagic cell death in non-small cell lung cancer NCI-H460 cells, Biochem. Biophys. Res. Commun. 337 (1) (2005) 52–60.
[60] G. Zhou, Y. Li, Y. Ma, Z. Liu, L. Cao, D. Wang, S. Liu, W. Xu, W. Wang, Size-dependent cytotoxicity of yttrium oxide nanoparticles on primary osteoblasts in vitro, J. Nanoparticle Res. 18 (2016) 1–14.
[61] M. Seguchi, P. Baumann-Zumstein, A. Fubel, R. Waksman, M. Haude, S. Galli, M. Joner, Preclinical evaluation of the degradation kinetics of third-generation resorbable magnesium scaffolds, Eurointervention: J. Europcr Collab. Working Group Int. Cardiol. European Soc. Cardiol. 19 (2) (2023) e167–e175.
[62] H. Yang, F. Zhang, J. Qian, J. Chen, J. Ge, Restenosis in Magmaris stents due to significant collapse, JACC Cardiovasc. Interv. 11 (10) (2018) e77–e78.
[63] R.N. Haddad, A. Adel Hassan, M. Al Soufi, M. Kasem, A word of caution: early failure of Magmaris® bioresorbable stent after pulmonary artery stenting, Cathet. Cardiovasc. Interv. 101 (1) (2023) 131–134.
[64] R. Menze, B. Hesse, M. Kusmierczuk, D. Chen, T. Weitkamp, S. Bettink, B. Scheller, Synchrotron microtomography reveals insights into the degradation kinetics of bio-degradable coronary magnesium scaffolds, Bioact. Mater. 32 (2024) 1–11.